Inorganic Chemistry
Article

Inorg. Chem. **2010**, *49*, 5503–5514 **5503**
DOI: 10.1021/ic1002012

Orientation and Stereodynamic Paths of Planar Monodentate Ligands in Square Planar Nickel N_2S Complexes

Roxanne M. Jenkins, Michael L. Singleton, Lauren A. Leamer, Joseph H. Reibenspies, and Marcetta Y. Darensbourg*

Department of Chemistry, Texas A&M University, College Station, Texas 77843

Received February 1, 2010

The well-established presence of histidine donors in binding sites of Ni-containing biomolecules prompts the study of orientational preference and stereodynamic nature of flat monodentate ligands (L = imidazoles, pyridine and an *N*-heterocyclic carbene) bound to planar N_2SNi moieties. Square planar $[N_2SNiL]^{n+}$ complexes are accessed through bridge-splitting reactions of dimeric, thiolate-S bridged $[N_2SNi]_2$ complexes. The solid state molecular structures of three mononuclear products, and three monothiolate bridged dinickel complexes, reveal that the plane of the added monodentate ligand orients largely orthogonal to the N_2SNiL square plane. Variable temperature ^1H NMR characterization of dynamic processes and ground state isomer ratios of imidazole complexes in their stopped exchange limiting spectra, readily correlate with density functional theory (DFT)-guided interpretation of Ni−L rotational activation barriers. Full DFT characterization finds Ni−L bond lengthening as well as a tetrahedral twist distortion in the transition state, reaching a maximum in the NHC complex, and relating mainly to the steric hindrance derived both from the ligand and the binding pocket. In the case of the imidazole ligands a minor electronic contribution derives from intramolecular electrostatic interactions (imidazole C-2 $C-H^{\delta+}$- - $S^{\delta-}$ interaction). Computational studies find this donor−acceptor interaction is magnified in O-analogues, predicting coplanar arrangements in the ground state of $N_2ON_{imid}Ni$ complexes.

Introduction

The orientational binding preferences and fluxional processes of ligands in transition metal complexes is an area of fundamental significance relating to catalysis and reactivity.[1−3] In the case of biologically relevant ligands such as imidazole, the study of these processes purports to offer insight into a vast array of biological systems containing metal bound histidine residues. Much of the effort in this area has been directed toward understanding His-heme iron interactions through the use of simple imidazoles as mimics of histidine.[4−12] These works have demonstrated that the axially ligated imidazole geometry (orientation of the plane of the imidazole with respect to the $Fe-N_{porphyrin}$ bond vectors, and tilt of the imidazole plane) can influence spectral changes,[4−6,12] shifts in redox properties,[6,7] coordination of substrates,[8] and changes in the spin state.[4]

Adding to the importance of $Fe-N_{histidine}$ interactions is a wide range of biological metal-bound histidine complexes that could have orientational consequences, specifically the Ni-containing imidazole metal binding sites found in Ni superoxide dismutase or NiSOD, and the transcription factor, NikR.[13−15] The orientation of histidine donors in

*To whom correspondence should be addressed. E-mail: marcetta@mail.chem.tamu.edu.

(1) Kolb, H. C.; Andersson, P. G.; Sharpless, K. B. *J. Am. Chem. Soc.* **1994**, *116*, 1278–1291.
(2) Evans, D. A.; Campos, K. R.; Tedrow, J. S.; Michael, F. E.; Gagné, M. R. *J. Am. Chem. Soc.* **2000**, *122*, 7905–7920.
(3) Leitner, A.; Shekhar, S.; Pouy, M. J.; Hartwig, J. F. *J. Am. Chem. Soc.* **2005**, *127*, 15506–15514.
(4) Scheidt, W. R.; Chipman, D. M. *J. Am. Chem. Soc.* **1986**, *108*, 1163–1167.
(5) Yatsunyk, L. A.; Dawson, A.; Carducci, M. D.; Nichol, G. S.; Walker, F. A. *Inorg. Chem.* **2006**, *45*, 5417–5428.
(6) Walker, F. A.; Huynh, B. H.; Scheidt, W. R.; Osvath, S. R. *J. Am. Chem. Soc.* **1986**, *108*, 5288–5297.
(7) Safo, M. K.; Walker, F. A.; Raitsimring, A. M.; Walters, W. P.; Dolata, D. P.; Debrunner, P. G.; Scheidt, W. R. *J. Am. Chem. Soc.* **1994**, *116*, 7760–7770.
(8) Menyhárd, D. K.; Keserú, G. M. *J. Am. Chem. Soc.* **1998**, *120*, 7991–7992.
(9) Safo, M. K.; Nesset, M. J. M.; Walker, F. A.; Debrunner, P. G.; Scheidt, W. R. *J. Am. Chem. Soc.* **1997**, *119*, 9438–9448.
(10) Zarić, S. D.; Popović, D. M.; Knapp, E.-W. *Biochemistry* **2001**, *40*, 7914–7928.
(11) Galstyan, A. S.; Zarić, S. D.; Knapp, E.-W. *J. Biol. Inorg. Chem.* **2005**, *10*, 343–354.
(12) Silvernail, N. J.; Roth, A.; Schulz, C. E.; Noll, B. C.; Scheidt, W. R. *J. Am. Chem. Soc.* **2005**, *127*, 14422–14433.
(13) Wuerges, J.; Lee, J.; Yim, Y.; Yim, H.; Kang, S.; Carugo, K. D. *PNAS.* **2004**, *101*, 8569–8574.
(14) Barondeau, D. P.; Kassmann, C. J.; Bruns, C. K.; Tainer, J. A.; Getzoff, E. D. *Biochemistry* **2004**, *43*, 8038–8047.
(15) Schreiter, E. R.; Sintchak, M. D.; Guo, Y.; Chivers, P. T.; Sauer, R. T.; Drennan, C. L. *Nat. Struct. Biol.* **2003**, *10*, 794–799.

Published on Web 05/27/2010

nickel-binding sites in such systems has not thus far been emphasized in structural studies.

Imidazole orientational binding preferences have been studied in square planar platinum complexes and octahedral ruthenium complexes.[16−19] Alessio, Marzilli, and co-workers explored octahedral Ru(II) complexes that contained aromatic N-donor, "lopsided" ligands such as 1,5,6-trimethylbenzimidazole, Me_3Bzm, and concluded that opposing forces between steric and electrostatic interactions affected ligand orientation and observed dynamic processes.[16] The variable temperature ^{1}H NMR spectra of *cis*,*cis*,*cis*-$RuCl_2(DMSO)_2$-$(Me_3Bzm)_2$ found that one Me_3Bzm ligand readily flips between two identified species (each isomer rotated 180° from the another) while the second Me_3Bzm ligand is immobile between −100 and +35 °C. The preferred, fixed orientation of the latter was attributed to electrostatic interactions between the $C-H^{\delta+}$ of Me_3Bzm and the two *cis* halides.[16] Other investigations by Velders, Reedijk, et al. of Ru−N bound substituted imidazoles in dicationic Ru^{2+} complexes that lack coordinated halides established that the observed rotational behavior of the imidazole ligands about the $Ru-N_{imid}$ bond is controlled exclusively by steric interactions.[19]

The orientation and rotational fluxionality of *N*-heterocyclic carbene (NHC) ligands have also been carefully studied, concluding that rotation of NHCs about the $M-C_{NHC}$ bond is also determined largely, and in most cases solely, by steric effects.[20−28] For square planar d^8 complexes the steric interference of NHC ligands with ancilliary ligands dictates the NHC ligand plane to orient nearly perpendicular to the metal ligand plane.[21,25−29]

Our work has employed diazacycles such as diazacycloheptane (dach) as support for pendant thiolate arms in development of N_2S_2 and N_2S multidentate ligands. The dach frame has been particularly amenable to the production of a monothiolate N_2S ligand, which upon reaction with nickel readily forms a dimeric, dithiolate-bridged Ni^{II} dication as precursor to monomeric cyano and imidazole complexes.[30,31] The $\mu_2(SR)_2$-bridged Ni^{II} dimer/ligand cleavage approach has also been used by Gale, Patra, and Harrop to produce monomeric $N_2SS'Ni$ complexes designed as NiSOD analogues,[32] and extensive syntheses based on cleavage reactions of $(S-N-S)_2Ni_2$ complexes were recently reported by Huang, Holm, et al.[29]

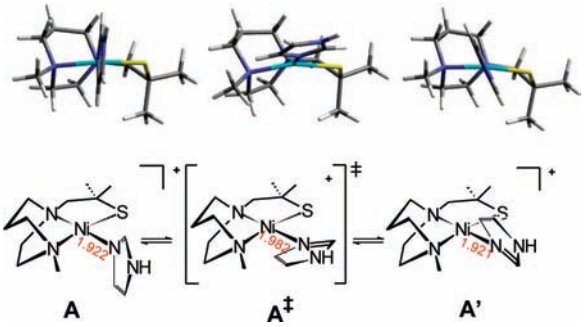

Figure 1. Left to right: **A**, DFT-calculated ground state structure of complex **A**; **A**‡, DFT-calculated transition state structure of complex **A** en route to isomer **A**′; Td twist (angle of intersection of N_2Ni and $N'SNi$ planes) of **A** = 7.9°, of **A**‡ = 21.2°.[31].

Solution phase investigations using ^{1}H NMR spectroscopy demonstrated that, because of the unsymmetric dach framework, isomers of the $(N_2SN')Ni$ complex **A**, Figure 1, existed at low temperatures in nearly equal ratio.[31] The observed equilibration of up/down orientations of the imidazole (with respect to the 6-membered nickel diazacycloheptane ring), isomers **A** and **A**′, was assigned to the rotation of the imidazole ligand about the $Ni-N_{imidazole}$ bond. The rotational barrier, ∼8.9 kcal/mol, was derived from analysis of the VT ^{1}H NMR data. Density Functional Theory (DFT) analysis of the ground state and transition state structures, complexes **A** and **A**‡, indicated for the latter a 0.06 Å increase in the $Ni-N_{imidazole}$ bond distance in addition to a significant deviation from square planarity as shown in Figure 1.[31] To explore the generality of this result and to provide insight into the factors contributing to the ground state imidazole binding orientation and to transition states of dynamic ligand rotational processes, a broader series of $[(N_2S)Ni]_2$ cleavage products containing planar ligands (imidazoles, pyridine, and an *N*-heterocyclic carbene) has been prepared. As the π-accepting/π-donating abilities of the added ligands are insignificant in these strong σ donors, the orientation of the monodentate ligand is dictated largely by minimization of steric interactions of L with the steric constraints of the N_2SNi binding site. Nevertheless, DFT computations suggest an intramolecular donor/acceptor interaction between the imidazole C−H and the thiolate S is operative in determining the stability of the ground state and transition state structures. A structural survey of square planar imidazole Ni complexes of tridentate ONO, ONN, ONS, and NNS

(16) Alessio, E.; Calligaris, M.; Iwamoto, M.; Marzilli, L. G. *Inorg. Chem.* **1996**, *35*, 2538–2545.
(17) Alessio, E.; Zangrando, E.; Roppa, R.; Marzilli, L. G. *Inorg. Chem.* **1998**, *37*, 2458–2463.
(18) Velders, A. H.; Hotze, A. C. G.; van Albada, G. A.; Haasnoot, J. G.; Reedijk, J. *Inorg. Chem.* **2000**, *39*, 4073–4080.
(19) Velders, A. H.; Quiroga, A. G.; Haasnoot, J. G.; Reedijk, J. *Eur. J. Inorg. Chem.* **2003**, 713–719.
(20) Doyle, M. J.; Lappert, M. F. *J. Chem. Soc., Chem. Commun.* **1974**, 679–680.
(21) Herrmann, W. A.; Gooβen, L. J.; Spiegler, M. *J. Organomet. Chem.* **1997**, *547*, 357–366.
(22) Weskamp, T.; Schattenmann, W. C.; Spiegler, M.; Herrmann, W. A. *Angew. Chem., Int. Ed.* **1998**, *37*, 2490–2493.
(23) Enders, D.; Gielen, H. *J. Organomet. Chem.* **2001**, *617−618*, 70–80.
(24) Chianese, A. R.; Li, X.; Janzen, M. C.; Faller, J. W.; Crabtree, R. H. *Organometallics* **2003**, *22*, 1663–1667.
(25) Silva, L. C.; Gomes, P. T.; Veiros, L. F.; Pascu, S. I.; Duarte, M. T.; Namorado, S.; Ascenso, J. R.; Dias, A. R. *Organometallics* **2006**, *25*, 4391–4403.
(26) Huang, J.; Schanz, H.-J.; Stevens, E. D.; Nolan, S. P. *Organometallics* **1999**, *18*, 2370–2375.
(27) Mata, J. A.; Chianese, A. R.; Miecznikowski, J. R.; Poyatos, M.; Peris, E.; Faller, J. W.; Crabtree, R. H. *Organanometallics* **2004**, *23*, 1253–1263.
(28) Brissy, D.; Skander, M.; Retailleau, P.; Marinetti, A. *Organometallics* **2007**, *26*, 5782–5785.
(29) Huang, D.; Deng, L.; Sun, J.; Holm, R. H. *Inorg. Chem.* **2009**, *48*, 6159–6166.
(30) Grapperhaus, C. A.; Bellefeuille, J. A.; Reibenspies, J. H.; Darensbourg, M. Y. *Inorg. Chem.* **1999**, *38*, 3698–3703.
(31) Jenkins, R. M.; Singleton, M. L.; Almaraz, E.; Reibenspies, J. H.; Darensbourg, M. Y. *Inorg. Chem.* **2009**, *48*, 7280–7293.
(32) Gale, E. M.; Patra, A. K.; Harrop, T. C. *Inorg. Chem.* **2009**, *48*, 5620–5622.
(33) Gou, S.; You, X.; Xu, Z.; Zhou, Z.; Yu, K. *Polyhedron* **1991**, *10*, 2659–2663.
(34) Mukhopadhyay, A.; Padmaja, G.; Pal, S.; Pal, S. *Inorg. Chem. Commun.* **2003**, *6*, 381–386.
(35) Ray, M. S.; Ghosh, A.; Mukhopadhyay, G.; Drew, M. G. B. *J. Coord. Chem.* **2003**, *56*, 1141–1148.
(36) Zhang, H.-H. *Acta Crystallogr.* **2006**, *E62*, m3110–m3111.

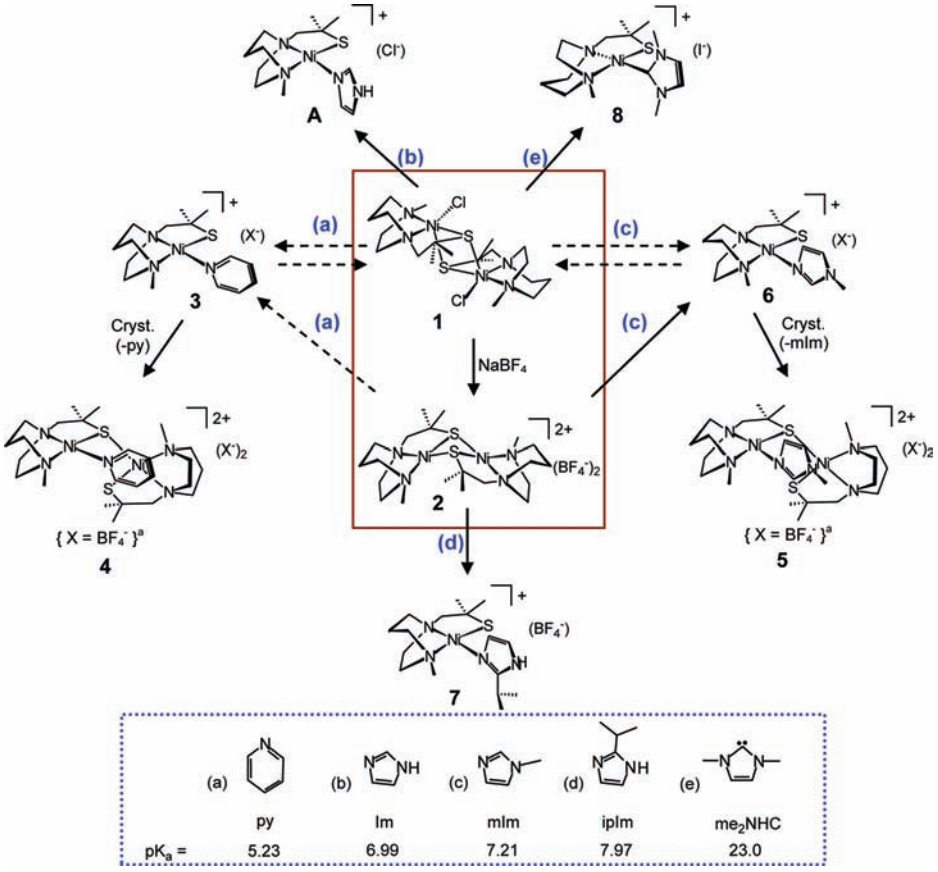

Figure 2. Summary of the dimer cleavage reactions of complexes **1** and **2** which yield mononuclear products **3** and **6**−**8** and monothiolate bridged dinickel complexes **4**−**5**. [a]Note: With BF_4^- counterion, the dinickel product forms during crystallization. Complex **A** was reported earlier.[31] Identification of ligands with respective pK_a values of the conjugate acids: (a) pyridine (py);[42] (b) imidazole (Im);[42] (c) 1-Methylimidazole (mIm);[43] (d) 2-Isopropylimidazole (ipIm);[43] and (e) dimethyl *N*-heterocyclic carbene (me_2NHC).[44] See Experimental Section for molar excesses of added ligands and for source of I^- in **8**.

Schiff base type ligands shows the importance of this effect in the presence of hard oxygen donors *cis* to the imidazole.[33−41]

Results and Discussion

Scope of the $Ni_2(\mu\text{-SR})_2$ Cleavage Reactions. Figure 2 displays the overall scope of the $Ni_2(\mu\text{-SR})_2$ cleavage reactions reported herein along with the pK_a values of the attacking ligands (as their conjugate acids) which vary from 5.23 to 23.[42−44] The exogenous ligands are largely planar in the coordination environment closest to the nickel, with steric properties imposed by substituents that flank the donor atom, described further below. The steric character of the nickel binding site is defined by a thiolate sulfur with two α-*gem* dimethyl groups and an N-donor from the diazacycloheptane frame. Given in Figure 3 are space-filling models derived from DFT computations, vide infra, of ground state structures of the square planar

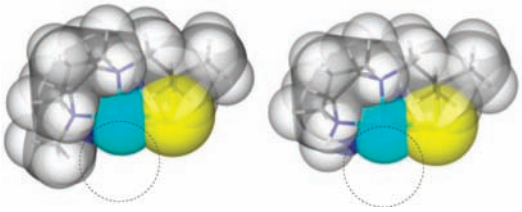

Figure 3. Space filling models of complexes **A** (left, based on mdach) and **9** (right, the dach derivative) in which the monodentate ligand has been removed, displaying the available open site that exists between the N- and S-donor sites.

complexes with the monodentate ligands removed so as to display the available binding site in complex **A** and in an analogue, complex **9**, in which the methyl substituent on the dach (mdach) is replaced with hydrogen (dach). While the methyl groups on the carbon α to the S-donor appear to have little steric influence on the ligands that dock into the available site on square planar nickel, the differences between complexes **A** and **9** are more substantial. This was experimentally confirmed by characterization of complexes **9** and **10** as prepared from dimeric complex **1-H**, Scheme 1.

Complexes **4**−**8**, **10**, and **A** in Figure 2 and Scheme 1 are represented according to their structures determined by X-ray crystallography. Complexes **3** and **9** are suggested to be analogous to other monomeric complexes consistent with their formulation by positive mode electrospray

(37) Mukhopadhyay, A.; Pal, S. *Eur. J. Inorg. Chem.* **2006**, 4879–4887.
(38) Chen, P.-K.; Shen, X.-Q.; Ge, C.-Y.; Kou, J.-F.; Zhang, H.-Y.; Hou, H.-W.; Zhu, Y.; Zheng, X.-F.; Zhang, H.-Q. *Synth. React. Inorg. Met-Org. Nano-Met. Chem.* **2006**, *36*, 603–607.
(39) Zhang, Q. L.; Zhu, B. X. *J. Coord. Chem.* **2008**, *61*, 2340–2346.
(40) Chen, X.-H. *Acta Crystallogr.* **2008**, *E64*, m1253.
(41) Salem, N. M. H.; El-Sayed, L.; Iskander, M. F. *Polyhedron* **2008**, *27*, 3215–3226.
(42) Lide, D. R. *CRC Handbook of Chemistry and Physics*; CRC Press: Boca Raton, Fl., 2000; pp 8−46 to 56.
(43) Lenarcik, B.; Ojczenasz, P. *J. Heterocycl. Chem.* **2002**, *39*, 287–290.
(44) Amyes, T. L.; Diver, S. T.; Richard, J. P.; Rivas, F. M.; Toth, K. *J. Am. Chem. Soc.* **2004**, *126*, 4366–4374.

Scheme 1

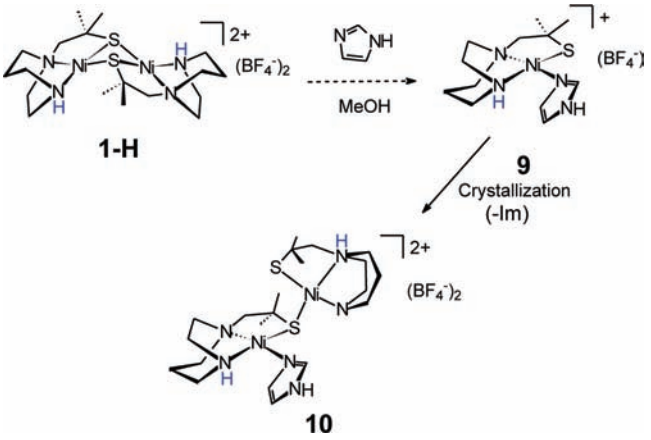

ionization mass spectrometry ($^{+}$ESI-MS) and physical properties (^{1}H NMR and UV−vis spectroscopies). A listing of all UV−vis data is given in Supporting Information, Table S1.

Monothiolate Bridged Dinickel Complexes: Reactions of Complexes 1 and 2 with py and mIm, Complexes 4 and 5, and of Complex 1-H with Im, Complex 10. As previously described, the addition of a slight excess of Im to [(mmp-mdach)NiCl]$_2$ (mmp-mdach = [1-(2-Mercapto-2-methyl-propyl)-methyl-1,4-diazacycloheptane]), complex **1**, yielded on precipitation with Et_2O a mononuclear Ni^{II} monocationic species, complex **A** in Figure 2, in high purity and yield.[31] The dimer cleavage reactions of **1** with py (a) and mIm (c) were initially performed following an identical protocol. As implied in Figure 2 there are complexities that relate to counterions in the syntheses and isolation of monomeric versus monothiolate bridged dinickel complexes. The isolation of the latter is a result of aggregation following the loss of one monodentate ligand during the crystallization process. The best approaches to the complexes of import to this study are given in the Experimental Section. Further descriptions of the equilibria involved in the cleavage processes of **1** with py and mIm are provided in the Supporting Information.

Complex **1-H** was chosen as a [(N$_2$S)Ni]$_2$ dimeric precursor to reduce the steric interference between the monodentate ligand and the dach N-donor in the mononuclear product, complex **9** (Scheme 1). Under the same conditions as used to produce complex **A**, complex **1-H** (either as its BF_4^- or Cl^- salt) reacted with excess Im in MeOH to yield an orange solid analyzed by $^{+}$ESI-MS, UV/vis spectroscopy, and ^{1}H NMR spectroscopy as complex **9**. X-ray quality crystals were obtained by the slow evaporation of complex **9** as its BF_4^- salt in MeOH; however, these crystals were found to be the monothiolate bridged dinickel species, complex **10**. As observed with complexes **4** and **5**, we conclude that the binuclear species forms during the crystallization process.

Molecular Structures of Monothiolate Bridged Dinickel Complexes. The molecular structures of complexes **4**, **5**, and **10** are shown in Figure 4 as ball and stick drawings, and selected metric data are compared in Supporting Information, Table S2. Thermal ellipsoid plots as well as crystallographic data are shown in the Supporting Information along with a description of the constraints

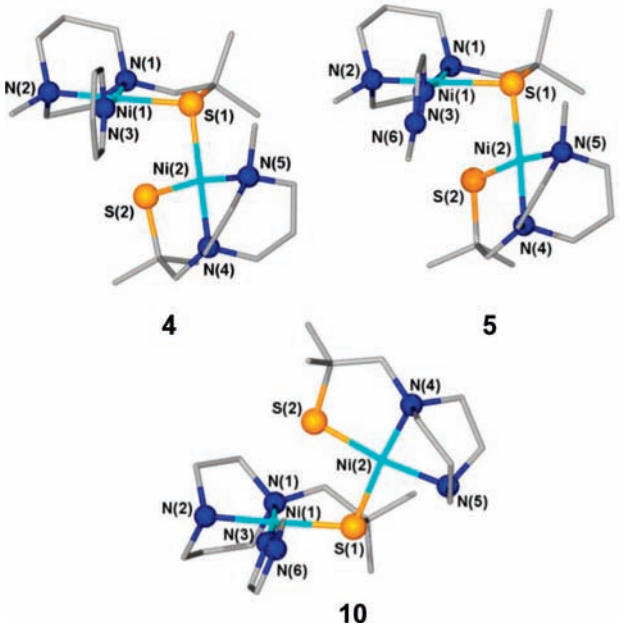

Figure 4. Ball and stick representation of complexes **4** (top left), **5** (top right), and **10** (bottom). The BF_4^- counterions are not shown. The asymmetric unit of complex **4** contains one MeCN of crystallization.

used in the refinement. Complexes **4**, **5**, and **10** consist of a Ni(μ-SR)Ni unit, in which both nickels are in a regular square planar geometry. The two square planes intersect with a dihedral angle of 81.4° for **4**, 77.8° for **5**, and 94.7° for **10**. Note that both **4** and **5** show that the exogenous N-donor ligand plane is orthogonal to the NiN$_2$N′S plane, while the imidazole ligand plane in **10** deviates from orthogonality by ~22°. This feature will be discussed later when the structures of the complete series are compared.

The Ni···Ni distances in **4**, **5**, and **10**, 3.379, 3.339, and 3.354 Å, respectively, are significantly longer than typical Ni···Ni distances in μ_2(SR)$_2$ butterfly complexes (2.7 to 2.9 Å).[30,31,45,46] The distances within the N$_2$N′SNi(1) plane are nearly identical for complexes **4**, **5**, and **10**, while the distances about Ni(2) show more deviation both between complexes **4**, **5**, and **10**, and as compared to analogous monomeric N$_2$S$_2$Ni compounds. As in all diazacycloheptane derivatives, the N−Ni−N angles are pinched to about 80°−82°, rendering the S−Ni−S angle or S−Ni−L angle ≥90°, as seen here. Overall, metric differences in the first coordination spheres of **4**, **5**, and **10** are minor.

Mononuclear Products: Reactions of Complexes 1 and 2 with mIm, ipIm, and me$_2$NHC; Complexes 6, 7, and 8. Isolation of single crystals of the fully cleaved mIm complex **6** in 42% yield was achieved upon the reaction of **2** with a 10-fold excess of mIm in addition to growing the orange-brown X-ray quality crystals in the presence of a further 5-fold excess of mIm in MeCN solution layered with Et_2O. A 3-fold excess of ipIm led to the full cleavage of complex **2**, yielding **7**, which was purified by precipitation with Et_2O. Diffraction-quality orange crystals of **7** were isolated from an Et_2O-layered solution of MeCN in

(45) Fackler, J. P., Jr. *Prog. Inorg. Chem.* **1976**, *21*, 55–90.
(46) Colpas, G. J.; Kumar, M.; Day, R. O.; Maroney, M. J. *Inorg. Chem.* **1990**, *29*, 4779–4788.

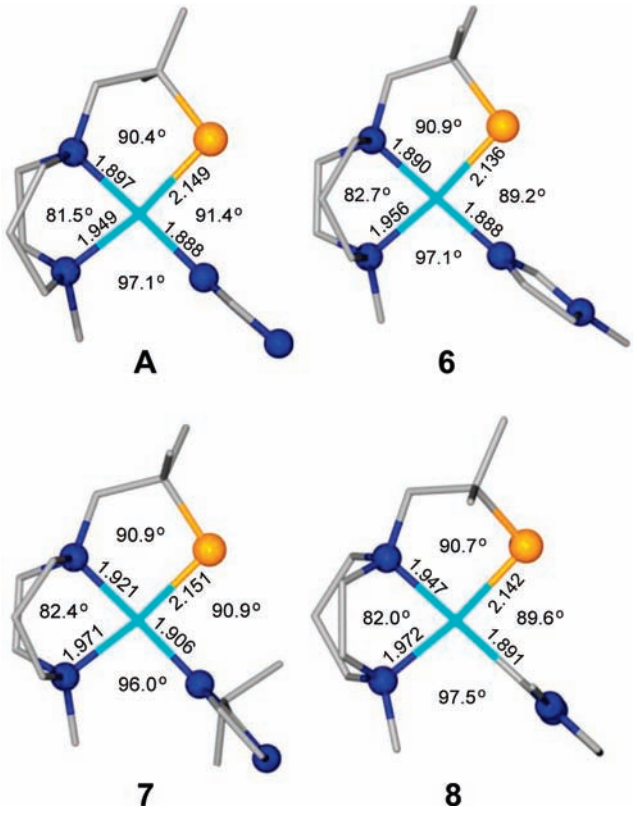

Figure 5. Structures of (mmp-mdach)Ni(Im)](Cl), **A**;[31] [(mmp-mdach)-Ni(mIm)]BF_4, **6**; [(mmp-mdach)Ni(ipIm)]BF_4, **7**; [(mmp-mdach)Ni(me_2-NHC)](I), **8**, with selected bond distances and angles. Counter anions are not shown. View ⊥ to the N_2S plane.

53% yield. The reaction of complex **2** with me_2NHC occurs readily in tetrahydrofuran (THF) solvent, and the pure product precipitated out of solution as the reaction proceeded. Complex **8** was isolated as an air stable, hygroscopic bright orange crystalline solid (46% yield) from the slow diffusion of Et_2O into a MeCN solution.

Molecular Structures of Mononuclear Products. Thermal ellipsoid plots of monocationic complexes **6**, **7**, and **8** and full structural reports are given in the Supporting Information along with a description of the restraints used in the refinement of complex **7**. Salient metric parameters are given within the ball and stick structures shown in Figure 5, and, for comparison, those of complex **A** are also given. The Ni−N_{dach} and Ni−S distances, and the N_{dach}−Ni−N_{dach} angles are largely the same in the four structures. The most significant difference is in the Ni−N_{dach} distance *trans* to the monodentate donor ligand that ranges from 1.890 to 1.947 Å, correlating with basicity of the *trans* ligand. The Ni−$C_{carbene}$ distance of 1.891 Å in **8** is the same as that reported by Huang, Holm, et al. for an NS_2Ni(carbene) complex in which the carbene donor is *trans* to pyridine.[29]

The critical feature for our study is the dihedral angle defined by the intersection of the exogenous monodentate ligand plane and the Ni complex plane, defined by the best N_2SNi$L_{donor\ atom}$ plane, Table 1. For the monomeric complexes, the ligands of greatest steric bulk (ipIm, **7**, and me_2NHC, **8**) are close to perpendicular to the nickel square plane, while the mIm derivative, complex **6**, is the furthest from 90°. The torsion angle that is defined in Table 1 is required for discussion in the computational section.

Table 1. Td Twist, Dihedral Angle between the Exogenous Ligand Plane and the N_2SNiL[a] Plane, and N−Ni−L−C2 Torsion Angle for Complexes **4**−**8**, **10**, and **A**

	4	**5**	**6**	**7**	**8**	**10**	**A**[31]
Td twist[b]	6.4°	5.7	4.1	6.8	4.9	1.7	7.9
dihedral angle[c]	86.6°	85.6	76.3	84.8	87.0	68.1	87.8
N−Ni−L−$C2_L$[d]	95.4°	90.6	108.3	93.2	91.1	117.2	95.0

[a] L = N donor atom in complexes **4**−**7**, **10**, and **A**, and L = C donor atom in complex **8**. [b] Td twist defined as the intersection of the N−Ni−N and the S−Ni−L planes. [c] Dihedral angle is defined as the angle between the N_2SNi−L plane and the best ligand plane. [d] *N* = nitrogen atom *cis* to L atom. For complexes **4** and **8**, $C2_L$ = atom α to the donor atom which is on the same side as the ethylene side of the dach backbone.

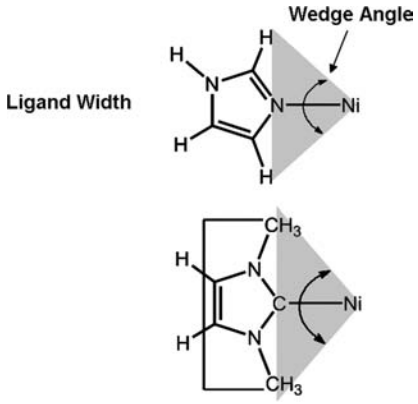

Figure 6. Illustration of ligand width and wedge angle used to define the steric bulk for flat ligands such as imidazoles and NHC's.

Defining the Steric and Electronic Contributions of the Ligands. Methods for describing steric and electronic properties of "flat" ligands such as *N*-heterocyclic carbenes have been well documented.[26,47] The donor properties of the ligands are typically compared by their effect on υ(CO) values in $LNi(CO)_3$ systems.[47] Because of the lack of spectroscopic reporter groups in our system, as well as the predominately σ donor character of N-donors in the *N*-heterocycles and the C-donor in NHC′s, we base the ligand donor ranking in these complexes on the pK_a of the donor atom's conjugate acid in each ligand, Figure 2.

The steric bulk of each ligand was evaluated from features in the experimentally and computationally determined structures. The ligand width was defined as the widest point closest to the metal center, Figure 6. For example, in the ipIm ligand this is the distance between the C5 imidazole proton and the proton on the tertiary carbon atom of the isopropyl substituent. The width as defined at this point on the ligand is more relevant to the steric encumbrance of the ligand within the coordination sphere than the larger width from the C5 proton to the isopropyl CH_3 groups as the latter orients away from the ligand metal system decreasing their steric effect. This effect is comparable to the smaller cone angle in phosphite ligands as defined by Tolman, et al.[48] The ligand wedge angle for flat ligands is defined as the angle made between the atoms that define the ligand width with the vertex being the Ni^{II} ion ($L_{donor\ atom}$−Ni avg. distance = 1.90 Å

(47) Gusev, D. G. *Organometallics* **2009**, *28*, 6458–6461.
(48) Tolman, C. A. *Chem. Rev.* **1977**, *77*, 313–348.

Table 2. Ligand Steric Parameters Taken from DFT Calculated Structures; Values from the X-ray Determined Structures Are Given in Parentheses

ligand	ligand width (Å)	wedge angle (deg)
Im, **A**	4.21 (3.94)	83.2 (78.0)
mIm, **6**	4.21 (3.98)	83.2 (79.2)
py, **3**[a]	4.14 (3.94)	91.3 (86.3)
ipIm, **7**	4.76 (4.69)	106.3 (101.6)
me_2NHC, **8**	5.04 (5.28)	121.9 (113.6)

[a] Experimental values were taken from structure of complex **5**.

(exp'tl); 1.92 (calc'd)). This definition is analogous to the A_L parameter described by Nolan and co-workers for comparison of steric properties of *N*-heterocyclic carbene ligands.[26] On the basis of these parameters, listed in Table 2, the ligands increase in steric bulk in the order: Im ~ mIm < py < ipIm < me_2NHC.

Defining the Barrier to Rotation about the Ni−L Bond of Complexes 6, 7, and 8: VT ^{1}H NMR. As was found for complex **A**,[31] the ^{1}H NMR spectra of the mIm analogue, complex **6**, change with temperature, Figure 7. In the imidazole C−H region, three ^{1}H resonances are observed at 22 °C and assigned according to the structure depicted within Figure 7. Resonances *a* and *b* broaden and reach coalescence on lowering the temperature to −60 °C, while resonance *c* remains sharp. By −80 °C, resonances *a* and *b* reappear as four distinct signals (*a*′ and *a*″ and *b*′ and *b*″), indicating the presence of two isomers. This behavior is almost identical to that of complex **A** and is to be expected as the added steric bulk of mIm is remote from the binding site. Free energy differences were obtained from K_{eq} values based on the isomer ratios at −80 °C and are calculated as in eqs 1 and 2.

$$K_{eq} = [a']/[a''] = 0.72 \quad (1)$$

$$\Delta G = -RT \ln K_{eq} = 0.14 \text{ kcal/mol} \quad (2)$$

The activation barrier, $\Delta G^{\ddagger}$, is obtained from the chemical shift difference between *a*′ and *a*″ ($\Delta\nu$ = 145 Hz) and the coalescence temperature (T_{coal} = −60 °C), eqs 3 and 4.

$$k_T = (\pi\Delta\nu/\sqrt{2}) = 322.1 \text{ s}^{-1} \quad (3)$$

$$\Delta G^{\ddagger} = -RT \ln(k_T h/k_b T_{coal}) = 9.0 \text{ kcal/mol} \quad (4)$$

The experimental barrier to rotation of 9.0 kcal/mol is, within experimental error, identical to that of complex **A** (8.9 kcal/mol).

The VT ^{1}H NMR spectra for the imidazole region of complex **7**, the ipIm derivative, in CD_3OD display two sets of doublets which indicate the presence of two isomers at 20 °C (Supporting Information, Figure S3). From the isomer ratio of *a*/*b* to *a*′/*b*′ observed at room temperature, the ΔG value was calculated to be 0.32 kcal/mol. To obtain spectra at higher temperatures, samples of **7** were explored in D_2O. These showed a similar spectrum at 20 °C as in the CD_3OD solution spectrum, with a more equal distribution of isomers (Figure 8). The pairs of singlets (*a* and *b* and *a*′ and *b*′) broaden and start to overlap near 100 °C. On cooling the sample back to 20 °C the two sets

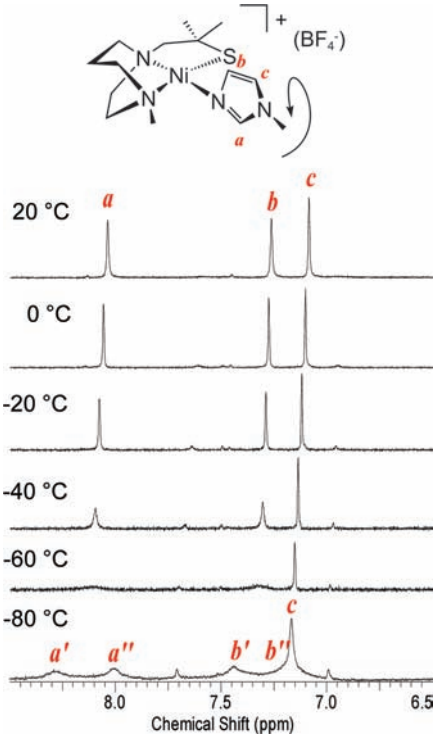

Figure 7. VT 500-MHz ^{1}H NMR spectra of complex **6** in CD_3OD.

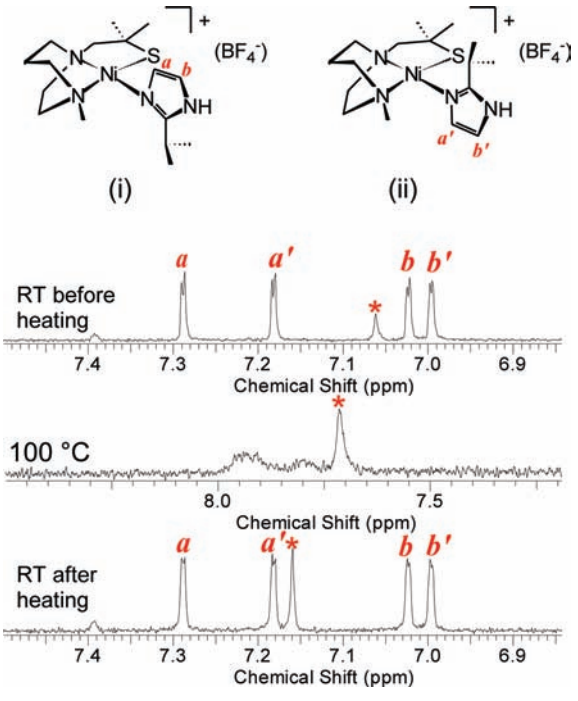

Figure 8. Top: Isomers of complex **7**; (i) is assigned as in the solid state by X-ray diffraction; (ii) the ipIm ligand is rotated 180° with respect to (i). Bottom: VT 500-MHz ^{1}H NMR spectra of complex **7** in D_2O. * = unbound ipIm.

of isomers, *a* and *b* and *a*′ and *b*′, reappear. Because the observed 'coalescence' temperature is at the experimental high temperature limit, it is unknown whether the spectral broadening is due to intra- or intermolecular exchange. Evidence for intermolecular exchange in complex **A** in the presence of free imidazole is presented below. Note that at

20 °C there is an additional resonance at 7.06 ppm, indicated by asterisk. This resonance shifts downfield as the temperature is raised, and unlike the resonance for bound ipIm, does not return to its original position on cooling back to 20 °C. However, free ipIm displays *a* resonance at 6.89 ppm, and the addition of free ipIm to **7** results in the disappearance of the additional signal indicated by asterisk and the emergence of a resonance at 6.89 ppm. Regardless of the starting position of the resonance indicated by asterisk, the addition of free ipIm results in only one signal positioned at 6.89 ppm. We conclude that the signal is most likely due to unbound ipIm, and the reason for the resonance shifts is not clear to us.

Complex **8**, the me_2NHC derivative, in CD_3OD at 20 °C shows an AB pattern that is centered at 7.18 ppm and assigned to C−H protons on the NHC ligand, and two singlets that are assigned to the NHC methyl groups at 4.37 and 4.38 ppm (Supporting Information, Figure S4). Upon heating the sample to ∼60 °C or cooling to −80 °C there are no changes in the spectra except for temperature dependent broadening and shifting (Supporting Information, Figure S5). This data implies that the NHC ligand does not rotate about the Ni−C bond in the tight confines of the square planar nickel fragment as would be expected for such a sterically hindered ligand of wedge angle = 122°; neither is there isomerization by dissociation/association. Steric repulsion between the NHC methyl group and the S atom as well as the NHC methyl group and the N-dach methyl group is expected to greatly destabilize the coplanar arrangement and results in a very high barrier to rotation.

The ^{1}H NMR spectrum of complex **9** at 20 °C displays three sharp singlets at 7.04, 7.09, and 7.86 ppm. These resonances are assigned, consistent with complex **A**, to the C−H protons on the coordinated imidazole ligand. At all temperatures explored (+60 to −80°), these signals remain sharp, but decrease in intensity with lowered temperatures as two additional sets of three singlets, of 1:1:1 ratios, appear. These completely reversible temperature-dependent spectra are shown in the Supporting Information, Figure S6. In view of the complicated dimer cleavage processes encountered during the syntheses, including monothiolate bridged dinickel materials such as those analogous to structures **4**, **5**, and **10**, the observation of other species is not surprising. While assignments of the other species would be extremely speculative, we can confidently conclude that the primary species is the mononuclear imidazole complex with rapid rotation about the $Ni-N_{imidazole}$ bond at all accessible temperatures. Similar results were noted in the spectra of complex **4** (Supporting Information, Figure S7). An activation energy barrier was obtained from these spectra; however, assignment to a monomeric or binuclear species is ambiguous.

Theoretical Predictions of ΔG and $\Delta G^{\ddagger}$ Values. DFT computations were carried out to calculate the free energies of (i) and (ii) isomers of complexes **3**−**4** and **6**−**9** and to predict the barriers for rotation about the Ni−L bond. Geometry optimizations were performed on each complex using the experimental X-ray molecular structure as the initial geometry (defined as isomer (i)). The metric data of the optimized structures were in good agreement with the experimentally determined results (Supporting Information, Table S6). A second optimized

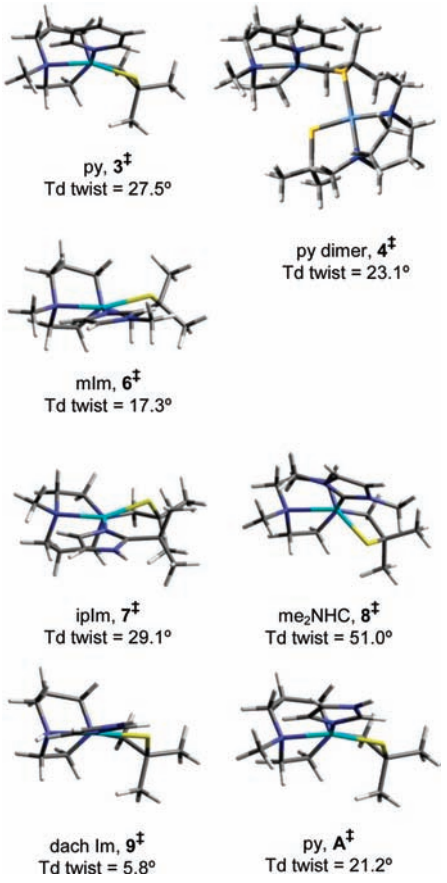

Figure 9. DFT optimized structures of the transition state geometries of complexes **3**, **4**, **6**−**9**, and **A**[31] showing the monodentate ligand planes in their maximum rotation position (ca. 90° from the ground state structure). Td twist values (defined as the intersection of the N−Ni−N and the $S-Ni-L_{donor}$ planes) are given below each structure.

structure for each complex was obtained from an initial geometry where the ligand is rotated 180° about the Ni−L bond vector (isomer (ii)). No other energy minima resulting from ligand rotation were found. The initial geometries of the transition state for each complex were located using the synchronous transit-guided quasi-Newton (QST2) method[49,50] utilizing the geometries for isomer (i) and isomer (ii) as the starting points. The transition state geometry of each complex shows the ligand plane to be largely perpendicular to its initial ground state orientation and roughly coplanar with the N_2SNi plane, Figure 9. The lowest energy transition state structure in the imidazole derivatives finds the imidazole C2 directed toward the S atom. To accommodate the transition state structure, the Ni-ligand bonds elongate, and there is also a significant increase in the tetrahedral twist of up to 46° (for example, in complex **8**, Td twist in the ground state structure equals 4.8°; in the transition state structure **8**‡, 51°). The important transition state structural parameters are provided in the Supporting Information, Figure S8.

In the transition state for complex **6**‡, the mIm ligand is rotated ∼59° from its position in ground-state **6**, with C2 of the imidazole pointed toward the S atom. To obtain this orientation the ligand drops out of the N_2S plane

(49) Peng, C.; Schlegel, H. B. *Isr. J. Chem.* **1994**, *33*, 449–454.
(50) Peng, C.; Ayala, P.; Schlegel, H. B.; Frisch, M. J. *J. Comput. Chem.* **1996**, *17*, 49–56.

Table 3. Experimental and DFT Calculated $\Delta G^{\ddagger}$ and ΔG Values for Complexes **3**, **4**, **6**−**9**, and **A** Based on the Rotation about the Ni−L Bond and Isomer Ratio Observed in the ^{1}H NMR Resonances[a]

N_2SLNi, L = ligand	$\Delta G_{expt'l}$	$\Delta G_{calc'd}$	$\Delta G^{\ddagger}_{expt'l}$	$\Delta G^{\ddagger}_{calc'd}$
Im(dach), **9**	unknown	0.37	n.a.[b]	3.29
Im(mdach), **A**[31]	0.11	0.18	8.90	8.86
mIm, **6**	0.15	0.13	8.97	8.95
py, **3**				14.04
py dinickel, **4**			11.23	17.82
ipIm, **7**	0.32	0.36	n.a.[b]	21.04
me_2NHC, **8**			n.a.[b]	29.93

[a] Values reported in kcal/mol. [b] Experimental $\Delta G^{\ddagger}$ value was not determined because of the constraints of the temperature range of the instrument or solvent used.

toward the ethylene side of the dach frame. This results in a distortion of the square planar geometry around the nickel giving a Td twist of 17°. This distortion is only slightly smaller than that found for complex $\mathbf{A}^{\ddagger}$ (21.2°)[31] and is consistent with the similar experimental barriers for rotation for complexes **A** and **6** (Table 3). This further corroborates that the slight difference in electronic character of the mIm over the Im ligand has little effect on the rotational barriers. In contrast, the decreased steric bulk around the Ni in the dach versus mdach complexes, see Figure 3, allows the imidazole ligand of complex $\mathbf{9}^{\ddagger}$ to bind in an orientation that is only 10° from coplanar with the N_2SNi plane, and the complex has a Td twist of only 5.8°. In the transition state structures containing the bulkier ligands, complexes $\mathbf{7}^{\ddagger}$ and $\mathbf{8}^{\ddagger}$, the distortion is much greater: $\mathbf{7}^{\ddagger}$ has a N−Ni−L−C2$_L$ torsion angle of 176.5° and a Td twist of 29.1° while the Td twist of the NHC-containing complex $\mathbf{8}^{\ddagger}$ is 51.0°. The severe distortions required to go through the transition state in both the ipIm and me_2NHC complexes correspond well with the high experimental barriers suggested for these complexes in the VT ^{1}H NMR spectra (Table 3).

Because of the possibility of an equilibrium between a monothiolate bridged dinickel complex and a mononuclear species in the case of complex **4**, the transition states for pyridine rotation were calculated for both $\mathbf{3}^{\ddagger}$ (Td twist = 27.5°; N−Ni−L−C2$_L$ torsion angle, where C2 = atom α to the donor atom which is on the same side as the ethylene side of the dach backbone = 178.3°) and $\mathbf{4}^{\ddagger}$ (Td twist = 23.1°; N−Ni−L−C2$_L$ torsion angle, = 175.6°). Despite these similarities, the energy barrier for py rotation is calculated to be significantly greater for the binuclear complex **4** (Table 3). However, the disparities between the experimental barrier and the calculated barriers for either the monomer or the dimer indicate that the process observed by NMR spectroscopy may be more complicated than ligand rotation in a single complex.

Table 3 lists the experimental and DFT-calculated ΔG and $\Delta G^{\ddagger}$ values for complexes **3**−**4**, **6**−**9**, and **A**. The predicted ΔG of 0.13 kcal/mol and $\Delta G^{\ddagger}$ of 8.95 kcal/mol for complex **6**, the mIm derivative, are consistent with the experimentally determined results and are nearly identical to complex **A**. In complex **7**, the ipIm derivative, the room temperature ^{1}H NMR spectrum indicated the presence of two species. The DFT-calculated ΔG for the two lowest energy conformations was found to be 0.36 kcal/mol, which compares well with the experimental value (based on the observed distribution or K_{eq}) of 0.32 kcal/mol. The large calculated barrier to rotation of 21.04 kcal/mol is due to the steric repulsion that is present when the ipIm ligand is roughly coplanar with N_2SNi plane. Consistently, the experimental $\Delta G^{\ddagger}$value could not be determined because of the temperature constraints of the solvent used. Likewise, rotation about the Ni−C bond was not observed in complex **8** over the temperature range studied, consistent with DFT-calculated activation barrier of 29.9 kcal/mol. In contrast, DFT predicts a low energy barrier ($\Delta G^{\ddagger}$) of 3.29 kcal/mol and a ΔG of 0.37 kcal/mol for complex **9**, the derivative with least steric hindrance. This barrier to rotation is substantially lower than that for complex **A**, and this DFT prediction is consistent with our inability to observe separate rotational isomers by NMR spectroscopy at the lowest accessible temperature. In the case of the pyridine complex the calculated rotational barriers for the monomer and the dinuclear complex were found to be higher than the experimentally determined value of 11.2 kcal/mol by ~3.0 and ~6.5, respectively.

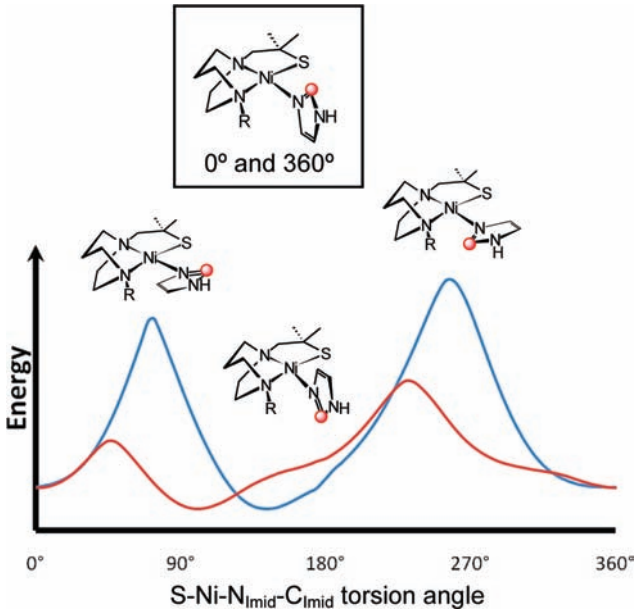

Figure 10. Plots of the potential energy of complexes **A** (R = CH_3) and **9** (R = H) as a function of the S−Ni−N$_{Imid}$−C$_{Imid}$ torsion angle. Blue: complex **A**; Red: complex **9**. The imidazole rotation starts from the optimized X-ray structure denoted as 0°.

Further evidence for steric control of dynamics is seen in comparisons of complexes **A** and **9**, which differ by the substituent on the terminal N donor of dach in the N_2SNi binding pocket, Figure 3. Relaxed potential energy scans monitor the change in potential energy of complexes **A** and **9** as a function of imidazole rotation, Figure 10. Note that two maxima result as the imidazole completes a 360° rotation. The first maximum, occurring as the C2C−H unit passes the thiolate S, is slightly lower than the second, resulting from the opposite orientation of the imidazole ligand dipole. This phenomenon is observed for both complexes, but is more dramatic for complex **9**. The large overall difference in the energy barriers for rotation between **A** and **9** is apparent by comparison at each energy maximum, and is consistent with the experimental and computational results for imidazole ligand rotation in **A** and **9**, Table 3.

Intermolecular vs Intramolecular Paths for Isomerization. The VT ^{1}H NMR studies demonstrated that stereoisomers

Complex	A-(S)	A-(O)	9-(S)	9-(O)
Ni-N_{imid},Å	1.923	1.938	1.916	1.926
Ni-S/O, Å	2.179	1.815	2.177	1.816
Dihedral Angle[a], °	84.4	41.9	58.5	14.0
N-Ni-N_{imid}-C2, °	102.5	140.8	125.9	194.1
S-Ni-N_{imid}-C2, °	82.8	38.4	58.9	-10.0

Figure 11. Overlays of computationally determined structures for (left) complex **A** as thiolate, (**A-(S)**), and as alkoxide, (**A-(O)**). Similarly (right), complex **9** as thiolate, (**9-(S)**), and as alkoxide, (**9-(O)**). In both overlays, the view is along the N_{imid}−Ni bond vector and shows tilt of the imidazole C2−H unit toward the chalcogen donor. In both overlays, the imidazole is in red for the alkoxide and in yellow for the thiolate derivative. [a]Pertinent metric parameters are given in the table, including dihedral angle of the ligand and complex planes as defined in the text, and torsion angles as noted.

of these complexes may coexist in solution, and, according to the good correlation between DFT calculations and the NMR data for complexes **A** and **6**, the isomerization process observed in certain N_2SLNi complexes is most reasonably assigned to intramolecular fluxionality, that is, rotation about the Ni−L bond. Nevertheless intermolecular isomerization processes are of concern, particularly in systems with high activation barriers as is the case of the two complexes containing the ligands of largest wedge angle, complexes **7** and **8**. The NHC ligands are known to be strongly coordinated to metal ions, and they show great stability toward thermal degradation in solution.[22,51]

As a probe of the possibility of intermolecular exchange, the VT ^{1}H NMR spectra of a well-characterized fluxional system, that of complex **A** was recorded in the presence of free imidazole. These data are presented and described in the Supporting Information, Figure S9. From them we conclude that intermolecular exchange processes indeed occur at $T > 10$ °C. However, the changes in the low temperature spectra are consistent with intramolecular exchange events.

Electrostatic Contributions to the Ground State Imidazole Binding Orientation. While the steric bulk of the ligands and interference with ancilliary or spectator ligands likely plays the largest role in the rotational barrier, there are slight deviations from orthogonality in the ground state orientation of the monodentate ligands in the less sterically bulky complexes, **A**, **6**, and **9** that appear to be of electrostatic origin. In all, the C2 position of the imidazole ligands, with its electropositive $C-H^{\delta+}$ tilts toward the thiolate S in both the experimental and the DFT calculated structures. This sort of internal electrostatic interaction has been surmised to be important in the orientation of axially coordinated imidazoles in heme systems.[10,11]

Indeed, a computational S/O replacement in complexes **A** and **9** resulted in greater deviation toward coplanarity for the alkoxide analogue of the thiolate. For example the C2 of imidazole orients toward the alkoxide $O^{\delta-}$, resulting in the case of computationally defined **9-(O)** an N−Ni−N_{imid}−$C2_{imid}$ torsion angle of 194°, that is, *a nearly coplanar imidazole/N_2ONiN_{imid} geometry*, Figure 11. In the case of complex **A-(O)**, with more steric hindrance built into the nickel binding pocket by virtue of the methyl group on the dach, the tilt of the imidazole in the *N_2ONiN_{imid}* is again roughly 40° away from the orthogonal orientation that is observed for the **A-(S)** derivative both experimentally and in the computations. In this case the Ni−N_{imid} bond lengthens by about 0.015 Å, presumably to accommodate the imidazole twist.

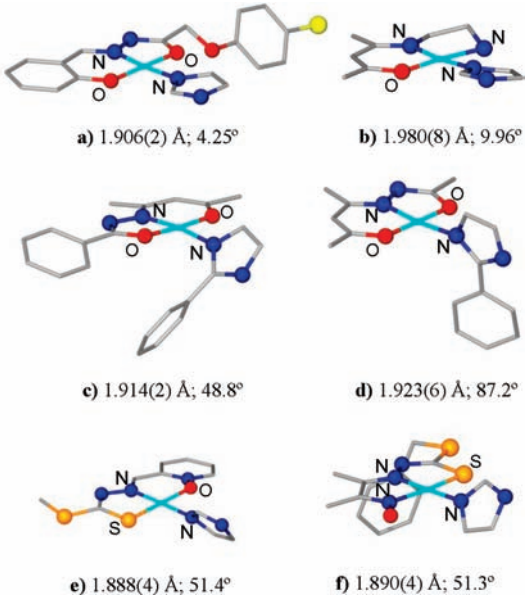

Figure 12. Selection of tridentate Schiff base ligand complexes of nickel with imidazoles in the fourth site. Ni−N_{imid} distances and dihedral plane defined as the angle between the best Ni square and imidazole plane given underneath each structure. (**a**) ref 40; (**b**) ref 35; (**c**) ref 37; (**d**) ref 37; (**e**) ref 33; (**f**) ref 41. Bond distances and angles are reported as averages for complexes containing more than one molecule in the asymmetric unit.

The conclusion that the shift toward coplanarity of imidazole and nickel planes in the N_2ONiN_{imid} virtual complexes is a result of an internal electrostatic interaction is consistent with the experimental structures of a set of square planar Ni^{II} complexes of tridentate, truncated Schiff base units that show greater variation in imidazole ligand orientation with respect to the tridentate ligand−metal plane. Ten such molecular structures are to be found in the Cambridge Crystallographic Database, six of which are shown in Figure 12; four others are given in Supporting Information, Figure S9.[33−41] None were characterized for imidazole fluxionality by VT NMR solution studies as in our study above. The Ni^{II}−Schiff base complexes containing hard O-donors *cis* to the unsubstituted imidazole monodentate ligand, complexes (a) and (b) in Figure 12, find coplanarity in the nickel complex plane and the plane of the imidazole ligand. Intramolecular H-bonding was reported in the interaction of the C2−H of the imidazole with the O-donor, and intermolecular H-bonding interactions involving the imidazole N−H define a one-dimensional assembly in the crystal lattice.[35,40] The four other structures of this type presented in Supporting Information, Figure S9 are also of the coplanar type.

With a sterically hindered imidazole ligand, molecular structures such as (c) and (d) of Figure 12 show substantial displacements of the imidazole ligand plane from the

(51) Schwarz, J.; Böhm, V. P. W.; Gardiner, M. G.; Grosche, M.; Herrmann, W. A.; Hieringer, W.; Raudaschl-Sieber, G. *Chem. Eur. J.* **2000**, *6*, 1773–1780.

nickel complex square plane inducing dihedral angles of about 49° and 87°, respectively.[37] Strong intermolecular H-bonding is seen in the extended molecular structures of both (c) and (d). In addition, complex (c) has an intramolecular C−H···π_{arene} interaction involving the ortho C−H group on the phenyl ring of the monodentate ligand and the phenyl ring of the tridentate ligand that is suggested to produce the observed canted orientation of the imidazole plane with respect to the metal square plane.[37] Complexes (e) and (f) in Figure 12 contain anionic S donors *cis* to the imidazole, and have intermediate metal-plane/ligand plane dihedral angles of about 50° with, in addition to the intermolecular interactions involving H-bonding of the imidazole N−H to an adjacent complex, an intramolecular interaction that points the C2 of the imidazole in the direction of the S atom of the tridentate ligand.[33,41]

Summary and Conclusion

Because of the asymmetry of the diazacycle frame in the complexes described above, an opportunity is presented to observe orientational preferences and dynamic rotational barriers that are influenced by the steric constraints of the ligand and the pocket into which flat ligands bind in square planar nickel complexes. While the imidazole ligand has the possibility of intramolecular donor/acceptor interactions, that is, the C2 $CH^{\delta+}$ with the thiolate $S^{\delta-}$, that would result in a canting of the imidazole toward the negatively charged donor atom, this interaction is very weakly expressed in the structures in our series. Thus we see an orientation of the imidazole plane that is largely orthogonal to the N_2SNi plane in the monomeric complexes, *determined principally by the optimization of minimal steric interactions while achieving maximum Ni−N_{imid} σ-bonding*.

The structural and dynamic results of our study, using N_2S binding sites, coupled with analysis of literature structures of various square planar nickel imidazole complexes in largely hard donor environment may be correlated as follows:

(1) In the Schiff base adducts consisting of N-, O-donor atoms the ground state imidazole binding orientation the reduced steric repulsion in the binding pocket that flanks the imidazole, and the significant intramolecular electrostatic interactions between O and the imidazole C2 $CH^{\delta+}$ overwhelm the minimal steric restrictions resulting in coplanarity. In the case of the N_2SNi complexes in the current study, increased steric bulk either on the binding pocket (the secondary and tertiary amines in the N_2S pocket) or on the planar monodentate ligand lead to a nearly perpendicular orientation of the imidazole plane, as intramolecular donor/acceptor interactions that would encourage canting of the imidazole ring toward coplanarity are minimal.

(2) While two isomers of the N_2SNi-N_{imid} complexes are seen at room and even higher temperatures (for imidazoles with steric hindrance at the C2 site), dynamic interconversions of nonhindered analogues occur with activation barriers experimentally accessible by VT NMR studies. The barriers obtained experimentally and through DFT studies show a correlation between increasing activation barrier and increasing steric hindrance, indicating that the mobility of the monodentate ligands about the Ni−L bond is controlled by the ligand size (width and wedge angle) and the access to nickel as controlled by the ancillary donors.

(3) The exchange of free and bound imidazole in complex **A**, occurs with a barrier of ∼11 kcal/mol and ceases close to 0 °C, further supporting that the exchange process observed for pure complex **A** at lower temperatures is a result of intramolecular dynamic processes.

(4) DFT optimized transition state structures for the interconversion of isomers of N_2SNi-N_{imid} find a lengthening of the $Ni-N_{imid}$ bond as rotation about the $Ni-N_{imid}$ bond pushes the imidazole into coplanarity with the nickel complex plane; distortion from strictly square planar further accommodates the increase in steric repulsion.

The orientation of His-imidazole in biological systems is influenced by many factors. This study has shown that two such factors, steric bulk and internal electrostatic interactions, determine the ground state binding orientation and dynamic behavior of *N*-heterocyclic ligands bound to square planar N_2S nickel sites, such as is found in the nickel responsive transcription factor, NikR.[15] The binding of four Ni^{2+} ions, each held in a square planar N_3SNi coordination environment, within the metal binding domain causes conformational changes in the protein superstructure, which initiates the interaction of the protein with DNA.[52] Fundamental model studies such as this one contribute to a delineation of the possible factors that may influence these protein structural and dynamic changes.

Experimental Section

General Procedures. All solvents used were purified and degassed via a Bruker solvent system. Anaerobic techniques, an argon-filled glovebox, and standard Schlenk techniques were employed. The starting material 1,3-bis(methyl)imidazolium iodide was prepared according to literature procedures.[53] Complexes **1**, **1-H**, and **A** were prepared as described previously.[30,31] All other reagents were purchased from Aldrich Chemical Co. and used as received.

Physical Measurements. Electronic absorption spectra were recorded on a Shimadzu UV-2450 spectrometer using quartz cells (1.00 cm path length). Mass spectrometry (ESI-MS) was performed by the Laboratory for Biological Mass Spectrometry at Texas A&M University. ^{1}H NMR analysis was carried out with a Mercury-300 FT-NMR spectrometer and variable temperature ^{1}H NMR spectra were acquired on an Inova500 spectrometer operating at 500 MHz. CD_3OD or D_2O were used as solvent and all resonances were referenced to MeOH (CH_3: 3.31 ppm) or D_2O (H_2O: 4.78), respectively, at all temperatures. Distinguishing resonances are reported for each complex. Atlantic Microlab, Inc., Norcross, Georgia, performed elemental analyses.

X-ray Crystal Structure Analyses. Low-temperature (110 K) X-ray data were obtained on a Bruker SMART 1000 CCD based diffractometer (Texas A&M University) (Mo sealed X-ray tube, Kα = 0.71073 Å) or on a Bruker-D8 Adv GADDS general-purpose three-circle X-ray diffractometer (Texas A&M

(52) Schreiter, E. R.; Wang, S. C.; Zamble, D. B.; Drennan, C. L. *Proc. Natl. Acad. Sci. U.S.A.* **2006**, *103*, 13676–13681.
(53) Chu, Y.; Deng, H.; Cheng, J.-P. *J. Org. Chem.* **2007**, *72*, 7790–7793.

University) (Cu sealed X-ray tube, Kα = 1.541 84 Å). Space groups were determined on the basis of systematic absences and intensity statistics. Structures were solved by direct methods and refined by full-matrix least-squares on F^2. H atoms were placed at idealized positions and refined with fixed isotropic displacement parameters and anisotropic displacement parameters were employed for all non-hydrogen atoms. The following programs were used: data collection, SMART WNT/2000 Version 5.632[54] or FRAMBO Version 4.1.05 (GADDS);[55] data reduction, SAINTPLUS Version 6.63;[56] absorption correction, SADABS;[57] cell refinement SHELXTL;[58] structure solutions, SHELXS-97 (Sheldrick);[59] and structure refinement, SHELXL-97 (Sheldrick).[60] The final data presentation and structure plots were generated in X-Seed Version 1.5.[61] Experimental conditions and crystallographic data are listed in the Supporting Information.

Computational Details. Initial geometries were derived from the X-ray structures. A second rotational isomer was found by using the same coordinates for the N_2SNi moiety as found in the X-ray structure but with the monodentate ligand rotated 180° about the Ni−$L_{donor\ atom}$ bond vector. These geometries were then optimized using DFT, with the Becke three-parameter exchange functional (B3)[62] and the Lee−Yang−Parr correlation functional(LYP) (B3LYP).[63]

All theoretical calculations, including optimization and frequency were performed with the Gaussian 03 suite programs.[64] The Stuttgart-Dresden[65] (SDD) effective core potential and valence basis set were used for nickel. For sulfur, the effective core potential and basis set of Hay and Wadt[66,67] were used with inclusion of a modified polarization function developed by Höllworth et al.[68] For nitrogen, the correlation-consistent polarized valence double-ζ basis set of Dunning and co-workers[69] (cc-pVDZ) was used. All carbon and hydrogen atoms were represented using the split valence double-ζ basis set of Pople and co-workers with polarization functions on heavy and light atoms[70−72] (6-31 g(d′,p′)).

Transition state geometries were calculated using the synchronous transit-guided quasi-Newton (QST2) method[49,50] with the final optimized geometries for both rotational isomers for each complex used as the initial and final geometries. Relaxed potential energy scans looking at rotation about the Ni−$L_{donor\ atom}$ were accomplished by freezing the S−Ni−$N_{imid/pyr}$−C2 or S−Ni−C_{NHC}−N_{NHC} torsion angles at 5° intervals and then allowing the rest of the molecule to optimize.

Syntheses and Isolation

[(mmp-mdach)Ni]$_2$[BF$_4$]$_2$, Complex 2. To a solution of 0.050 g (0.085 mmol) of [(mmp-mdach)NiCl]$_2$, complex **1**, in MeOH (20 mL) was added 0.019 g (0.173 mmol) of $NaBF_4$ in MeOH (15 mL); the solution was stirred overnight. Solvent was removed under vacuum, and MeCN (20 mL) was added, precipitating NaCl, and yielding a maroon solution of [(mmp-mdach)Ni]$_2$[BF$_4$]$_2$, complex **2**. The solution was filtered over Celite, solvent was removed in vacuo, and 0.055 g (93% yield) of pure complex **2** was isolated as a maroon solid. Absorption spectrum (MeOH): λ_{max} (ε, $M^{-1}\ cm^{-1}$) 525 (354), 418 (322), 280 (4138), 244 (7247) nm. $^+$ESI-MS (MeCN): m/z = 259 [(me-mdach)Ni]$_2^{2+}$.

[(mmp-mdach)Ni(py)][Cl], Complex 3. A mixture of 0.030 g (0.051 mmol) of **1** in MeOH (25 mL) with 12.0 μL (0.149 mmol) of pyridine was stirred overnight, producing a color change from wine to yellow-orange. As the solvent was removed in vacuo, the completely dried residue on the sides of the flask turned purple, while the solution changed to a deep orange. An additional 20.0 μL (0.248 mmol) of pyridine was added to the concentrated solution, stirred to mix the residue on the sides of flask, yielding a dark orange solution. Absorption spectrum of the reaction mixture (MeOH): λ_{max} 453, 350 (sh), 290, 255, 231 nm. $^+$ESI-MS (MeOH): m/z = 338, [(mmp-mdach)Ni(py)]$^+$.

py-[(mmp-mdach)Ni]$_2$[BF$_4$]$_2$, Complex 4. A mixture of 0.050 g (0.072 mmol) of **2** in MeCN (30 mL) with 21.8 μL (0.253 mmol) of pyridine, py, was stirred for 2 days, producing a color change from maroon to deep yellow. The solvent was reduced to a minimum followed by Et_2O diffusion (in the presence of a ∼2.5 equiv excess py) to yield X-ray quality crystals. Pure reddish-orange crystalline product was isolated in 54% yield (0.031 g). Elemental anal. for $Ni_2C_{25}H_{47}N_5S_2B_2F_8$ (MW = 773 g/mol), Calcd (found): C, 38.85 (38.29); N, 9.06 (8.88); H, 6.13 (6.09). Absorption spectrum (MeOH): λ_{max} (ε, $M^{-1}\ cm^{-1}$) 502 (sh), 471 (344), 334 (sh), 291 (6976), 244 (8345) nm. $^+$ESI-MS (CH_2Cl_2:MeOH): m/z = 684, py-[-(mmp-mdach)Ni)]$_2BF_4^+$; 338, [(mmp-mdach)Ni(py)]$^+$; 259, [(me-mdach)Ni]$_2^{2+}$.

mIm-[(mmp-mdach)Ni]$_2$[BF$_4$]$_2$, Complex 5, and [(mmp-mdach)Ni(mIm)][BF$_4$], Complex 6. Method A. To a maroon solution of **2** (0.073 g, 0.105 mmol) in MeOH (30 mL) was added a colorless solution of 1-Methylimidazole, mIm, (30 μL, 0.376 mmol) in MeOH (10 mL), which produced an orange solution. After stirring overnight, the solution volume was reduced to a minimum under vacuum, and Et_2O was added to precipitate the product. The ether was decanted, the product was washed with Et_2O (3 × 25 mL), and the resulting orange product was dried in vacuo. Absorption spectrum (MeOH): λ_{max} (ε, $M^{-1}\ cm^{-1}$) 467 (319), 341 (sh), 290 (6534), 225 (8097) nm. $^+$ESI-MS (MeOH): m/z = 341 [(mmp-mdach)Ni(mIm)]$^+$. The orange solid was dissolved in MeCN and layered with Et_2O. At 5 °C, diffusion of Et_2O into the MeCN solution that

(54) *SMART V5.632 Program for Data Collection on Area Detectors*; Bruker AXS Inc.: Madison, WI, 1999.
(55) *FRAMBO:FRAME Buffer Operation Version 41.05 Program for Data Collection on Area Detectors*; Bruker AXS Inc.: Madison, WI, 1999.
(56) *SAINT V6.63 Program for Reduction of Area Detector Data*; Bruker AXS Inc.: Madison, WI, 1999.
(57) Sheldrick, G. *SADABS Program for Absorption Correction Area Detector Frames*; Bruker AXS Inc.: Madison, WI, 1999.
(58) Sheldrick, G. *SHELXTL-PLUS, Version 4.11V, SHELXTL-PLUS Users Manual*; Siemens Analytical X-ray Instruments, Inc.: Madison, WI, 1990.
(59) Sheldrick, G. *SHELXS-97, Program for Crystal Structure Solution*; Institut fur Anorganische Chemie der Universität Göttingen: Göttingen, Germany, 1997.
(60) Sheldrick, G. *SHELXL-97, Program for Crystal Structure Refinement*; Institut fur Anorganische Chemie der Universität Göttingen: Göttingen, Germany, 1997.
(61) Barbour, L. J. *J. Supramol. Chem.* **2001**, *1*, 189–191.
(62) Becke, A. D. *J. Chem. Phys.* **1993**, *98*, 5648–5652.
(63) Lee, C.; Yang, W.; Parr, R. G. *Phys. Rev.* **1988**, *37*, 785–789.
(64) All calculations were carried out with the Gaussian 03 program: Frisch, M. J. et al. *Gaussian 03*, revision C.02; Gaussian Inc.: Wallingford, CT, 2004. See Supporting Information for the full reference.
(65) Dolg, M.; Wedig, U.; Stoll, H.; Preuss, H. *J. Chem. Phys.* **1987**, *86*, 866–872.
(66) Hay, P. J.; Wadt, W. R. *J. Chem. Phys.* **1985**, *82*, 284–398.
(67) Hay, P. J.; Wadt, W. R. *J. Chem. Phys.* **1985**, *82*, 270–283.
(68) Höllwarth, A.; Böhme, M.; Dapprich, S.; Ehlers, A. W.; Gobbi, A.; Jonas, V.; Köhler, K. F.; Stegmann, R.; Veldkamp, A.; Frenking, G. *Chem. Phys. Lett.* **1993**, *208*, 237–240.
(69) Dunning, T. H., Jr. *J. Chem. Phys.* **1989**, *90*, 1007–1023.
(70) Hehre, W. J.; Ditchfield, R.; Pople, J. A. *J. Chem. Phys.* **1972**, *56*, 2257–2261.
(71) Hariharan, P. C.; Pople, J. A. *Theor. Chim. Acta* **1973**, *28*, 213–222.
(72) The d′,p′ functions are the exponents from the 6-311G(d,p) basis set: Krishnan, R.; Binkley, J. S.; Seeger, R.; Pople, J. A. *J. Chem. Phys.* **1980**, *72*, 650–654.

contains complex **6** gave small yellow-orange needles initially and within 2 days changed into red-orange block crystals (12 mg, 15%) indentified by X-ray crystallography not as **6** but rather the dinuclear mIm-[(mmp-mdach)Ni]$_2$-[BF$_4$]$_2$, complex **5**. Elemental anal. for $Ni_2C_{24}H_{48}N_6S_2B_2F_8 \cdot MeCN$ (MW = 817 g/mol), Calcd (found): C, 38.23 (38.91); N, 12.03 (12.17); H, 6.29 (6.58). $^+$ESI-MS (CH_2Cl_2:MeOH): m/z = 687, mIm-[(mmp-mdach)Ni)]$_2$BF$_4^+$; 341, [(mmp-mdach)Ni(mIm)]$^+$; 259, [(me-mdach)Ni]$_2^{2+}$.

Method B. To a maroon solution of **2** (0.035 g, 0.050 mmol) in MeCN (25 mL) was added a colorless solution of mIm (41 μL, 0.514 mmol) in MeCN (10 mL), which immediately produced an orange solution. After stirring overnight, the solution volume was reduced to a minimum under vacuum, and additional neat mIm (30 μL, 0.376 mmol) was added. The solution was filtered, and the filtrate was layered with Et_2O to deposit orange-brown crystalline product (0.018 g, 42% yield) identified as the mononuclear product [(mmp-mdach)Ni(mIm)][BF$_4$], complex **6**. Elemental anal. for $NiC_{14}H_{27}N_4SBF_4$ (MW = 429 g/mol), Calcd (found): C, 39.20 (39.21); N, 13.10 (12.97); H, 6.34 (6.34). Absorption spectrum (MeOH): λ_{max} (ε, M^{-1} cm^{-1}) 467 (319), 341 (sh), 290 (6534), 225 (8097) nm. $^+$ESI-MS (MeOH): m/z = 341 [(mmp-mdach)Ni(mIm)]$^+$. ^{1}H NMR (500 MHz, CD_3OD) δ 8.04 (s, 1H), 7.26 (s, 1H), 7.09 (s, 1H), 3.70 (s, 3H), 1.69 (s, 3H), 1.60 (s, 3H), 1.38 (s, 3H).

[(mmp-mdach)Ni(ipIm)][BF$_4$], Complex 7. A solution of 2-Isopropylimidazole, ipIm, (0.029 g, 0.264 mmol) in MeCN (10 mL) was added to a stirring maroon solution of **2** (0.061 g, 0.088 mmol) in MeCN (25 mL), resulting in an immediate color change to bright orange. After stirring overnight, the solution volume was reduced to a minimum under vacuum, and Et_2O was added to precipitate the product. The ether was decanted, the product was washed with Et_2O (3 × 25 mL) to remove excess ipIm, and dried in vacuo to afford the product as an orange solid (0.421 g, 53% yield). X-ray quality crystals were obtained by Et_2O diffusion into a MeCN solution. Elemental anal. for $NiC_{16}H_{31}N_4SBF_4 \cdot H_2O$ (MW = 475 g/mol), Calcd (found): C, 40.46 (40.97); N, 11.79 (11.79); H, 7.00 (6.68). Absorption spectrum (MeOH): λ_{max} (ε, M^{-1} cm^{-1}) 468 (189), 335 (sh), 290 (4190), 223 (4768) nm. $^+$ESI-MS (MeOH): m/z = 369 [(mmp-mdach)Ni(ipIm)]$^+$. ^{1}H NMR (500 MHz, CD_3OD) δ 7.33 (d, 1H), 7.23 (d, 1H), 7.04 (d, 1H), 7.01 (d, 1H).

[(mmp-mdach)Ni(me$_2$NHC)][I], Complex 8. 1,3-Bis-(methyl)imidazolium iodide (0.044 g, 0.196 mmol) and KOtBu (0.023 g, 0.205 mmol) were mixed and stirred in dry THF (15 mL) for 1 h. The mixture was then added in situ to a slightly soluble purple suspension of complex **1** (0.040 g, 0.068 mmol) in THF (25 mL) and stirred for 18 h. As the reaction proceeded the solution turned orange-red, and an orange solid precipitated. The solution was filtered, and the solid was washed with hexanes (3 × 25 mL). X-ray quality crystals were obtained by vapor diffusion of Et_2O into a MeCN solution. The bright orange crystalline material was collected yielding 0.030 g (46%). Elemental anal. for $NiC_{15}H_{29}N_4SI \cdot H_2O$ (MW = 501 g/mol), Calcd (found): C, 35.95 (35.56); N, 11.18 (11.08); H, 5.82 (6.24). Absorption spectrum (MeOH): λ_{max} (ε, M^{-1} cm^{-1}) 417 (104), 268 (2652), 233 (4148) nm. $^+$ESI-MS (MeOH): m/z = 355 [(mmp-mdach)Ni(me$_2$NHC)]$^+$. ^{1}H NMR (500 MHz, CD_3OD) δ 7.19−7.18 (dd, 2H), 4.37 (s, 3H), 4.38 (s, 3H), 1.92 (s, 3H), 1.62 (s, 3H), 1.39 (s, 3H).

[(mmp-dach)Ni(Im)][BF$_4^-$], Complex 9, and Im-[(mmp-dach)Ni]$_2$[BF$_4$]$_2$, Complex 10. To a solution of **1-H** (0.030 g, mmol) in MeOH (30 mL) was added a solution of imidazole, Im, (0.011 g, mmol) in MeOH (10 mL). The color of the solution immediately changed from red to orange. After stirring overnight, the solvent volume was reduced to a minimum, and the addition of Et_2O led to an orange precipitate, which was washed with Et_2O (3 × 25 mL). The solid was dissolved in CH_2Cl_2 and filtered over Celite, dried in vacuo, yielding (22 mg, 61%). Absorption spectrum (MeOH): λ_{max} (ε, M^{-1} cm^{-1}) 455 (59), 370 (sh), 282 (1319), 215 (3777) nm. $^+$ESI-MS (MeOH): m/z = 313 [(mmp-dach)Ni(Im)]$^+$. ^{1}H NMR (500 MHz, CD_3OD) δ 7.86 (s, 1H), 7.09 (s, 1H), 7.04 (s, 1H), 1.61 (s, 3H), 1.43 (s, 3H). Slow evaporation of a MeOH solution of complex **9** resulted in orange block crystals indentified by X-ray crystallography as a monothiolate bridged dinickel species, Im-[(mmp-dach)Ni(Im)][BF$_4$]$_2$, complex **10**, (16 mg, 48%). $^+$ESI-MS (CH_2Cl_2:MeOH): m/z = 645, Im-[(mmp-dach)Ni)]$_2$BF$_4^+$; 313, [(mmp-dach)Ni(Im)]$^+$; 245, [(me-dach)Ni]$_2^{2+}$.

Acknowledgment. We gratefully acknowledge the financial support of the National Science Foundation (CHE-0910679 to M.Y.D.) with contributions from the R. A. Welch Foundation (A-0924) and the National Institutes of Health (Chemistry-Biology Interface Training Grant to R.J., T32 GM008523). Extensive discussion with Prof. Michael B. Hall and Dr. Liza Perez are much appreciated. Lauren A. Leamer, University of Texas, Tyler, was an NSF-REU participant, summer 2009.

Supporting Information Available: Full description of monothiolate bridged dinickel complexes, UV−vis data, $^+$ESI-MS of the reaction mixture of **1** with **3** and **6**, full listing of metric parameters for **6**−**8**, selected experimental and optimized parameters for **4** and **6**−**8**, 500-MHz ^{1}H NMR spectrum of **4** and **7**−**9**, VT 500-MHz ^{1}H NMR spectra of the addition of free imidazole to **A**, Cartesian coordinates (Å) and DFT structures for **4** and **6**−**9**, plot of ln(k) versus $1/T$ for imidazole exchange in **A**, summary of crystallographic data for **4**−**8** and **10**, tridentate Schiff base ligand complexes of nickel with imidazoles in the forth site, and full citation for the Gaussian 03 program (ref 64). This material is available free of charge via the Internet at http://pubs.acs.org.